Solvent engineering of the Brownian tree-shaped lateral heterogeneity in 2D Ruddlesden–Popper perovskites: Resolving the trade-off between crystallinity and buried interface integrity

Biao Yang(杨彪), Yuxian An(安宇娴), Kenneth P. Ghiggino, Ziyang Hu(胡子阳), Fei Zheng(郑飞)
Citation: Chin. Phys. B. 35, 106803 (2026). DOI: 10.1088/1674-1056/aea53c | CSTR: 32038.14.CPB.aea53c
http://cpb.iphy.ac.cn; http://iopscience.iop.org/cpb

What follows is a list of articles you may be interested in

Formation of crystalline Si_9C_{15} nano-islands and Si_9C_{15}/graphene heterostructures on Ru(0001)

Lijing Huang(黄丽静), Yumeng Li(李雨萌), Hongqin Xiao(肖洪钦), Yuxuan He(何昱萱), Geng Li(李更), Hong-Jun Gao(高鸿钧)
Chin. Phys. B. 35, 056801 (2026). DOI: 10.1088/1674-1056/ae4c6f | CSTR: 32038.14.CPB.ae4c6f

Effects of Mg-doping temperature on the structural and electrical properties of nonpolar a-plane p-type GaN films

Kai Chen(陈凯), Jianguo Zhao(赵见国), Yu Ding(丁宇), Wenxiao Hu(胡文晓), Bin Liu(刘斌), Tao Tao(陶涛), Zhe Zhuang(庄喆), Yu Yan(严羽), Zili Xie(谢自力), Jianhua Chang(常建华), Rong Zhang(张荣), Youliao Zheng(郑有炓)
Chin. Phys. B. 33, 016801 (2024). DOI: 10.1088/1674-1056/acdc0b

Strain compensated type II superlattices grown by molecular beam epitaxy

Chao Ning(宁超), Tian Yu(于天), Rui-Xuan Sun(孙瑞轩), Shu-Man Liu(刘舒曼), Xiao-Ling Ye(叶小玲), Ning Zhuo(卓宁), Li-Jun Wang(王利军), Jun-Qi Liu(刘俊岐), Jin-Chuan Zhang(张锦川), Shen-Qiang Zhai(翟慎强), Feng-Qi Liu(刘峰奇)
Chin. Phys. B. 32, 046802 (2023). DOI: 10.1088/1674-1056/ac7cd4

Porous AlN films grown on C-face SiC by hydride vapor phase epitaxy

Jiafan Chen(陈家凡), Jun Huang(黄俊), Didi Li(李迪迪), Ke Xu(徐科)
Chin. Phys. B. 31, 076802 (2022). DOI: 10.1088/1674-1056/ac597e

Preparation of AlN film grown on sputter-deposited and annealed AlN buffer layer via HVPE

Di-Di Li(李迪迪), Jing-Jing Chen(陈晶晶), Xu-Jun Su(苏旭军), Jun Huang(黄俊), Mu-Tong Niu(牛牧童), Jin-Tong Xu(许金通), Ke Xu(徐科)
Chin. Phys. B. 30, 036801 (2021). DOI: 10.1088/1674-1056/abd392

SPECIAL TOPIC — A 40th Anniversary Celebration: Physics Research and Innovation at Ningbo University

Solvent engineering of the Brownian tree-shaped lateral heterogeneity in 2D Ruddlesden–Popper perovskites: Resolving the trade-off between crystallinity and buried interface integrity

Biao Yang(杨彪)[1], Yuxian An(安宇娴)[1], Kenneth P. Ghiggino[2], Ziyang Hu(胡子阳)[1,†], and Fei Zheng(郑飞)[1,‡]

[1] *Department of Microelectronic Science and Engineering, School of Physical Science and Technology, Ningbo University, Ningbo* 315211, *China*
[2] *School of Chemistry, The University of Melbourne, Parkville, Victoria* 3010, *Australia*

(Received 9 July 2026; revised manuscript received 6 September 2026; accepted manuscript online 10 September 2026)

Two-dimensional Ruddlesden–Popper perovskites (2D RPPs) are promising light absorbers for stable perovskite solar cells (2D-PSCs). However, the influence of lateral mesoscopic heterogeneity, particularly its correlation with buried-interface defects and photovoltaic performance, remains poorly understood. Here, we employ solvent engineering to tune the crystallization kinetics of 2D RPP films and investigate the evolution of Brownian tree-shaped lateral heterogeneity and its impact on buried-interface integrity and device performance. Increasing the DMSO fraction gradually delays crystallization, leading to improved crystallinity and preferred vertical orientation. Meanwhile, the Brownian tree-shaped domains progressively expand, accompanied by the development of interconnected void networks at the buried interface and reduced charge collection due to compromised buried-interface contact. An intermediate DMF:DMSO ratio of 8:2 achieves the optimal balance between crystalline quality and buried-interface integrity, yielding a champion power conversion efficiency of 17.63%. These findings demonstrate that balancing crystalline quality and buried-interface integrity is essential for achieving high-performance 2D-PSCs and other related optoelectronics.

Keywords: Ruddlesden–Popper perovskites, Brownian tree, crystalline morphology, lateral heterogeneity

PACS: 68.55.–a, 73.50.Pz, 88.40.H–

DOI: 10.1088/1674-1056/aea53c **CSTR:** 32038.14.CPB.aea53c

1. Introduction

Organic-inorganic hybrid perovskite solar cells (PSCs) have attracted extensive attention because of their excellent optoelectronic properties, including high absorption coefficients, tunable bandgaps, long carrier diffusion lengths, and low-temperature solution processability.[1–3] Although conventional three-dimensional (3D) perovskites have achieved remarkable power conversion efficiencies (PCEs), their long-term instability under moisture, oxygen, heat, light, and electrical bias remains a major obstacle to practical application.[4,5] Two-dimensional Ruddlesden–Popper perovskites (2D RPPs), formed by incorporating bulky organic spacer cations into the perovskite framework, provide an effective route to improve environmental and operational stability.[6,7] Their hydrophobic organic spacer layers can suppress moisture ingress and ion migration, making 2D RPPs promising candidates for stable photovoltaic devices.[8,9]

2D RPPs generally follow the formula $R_2A_{n-1}B_nX_{3n+1}$, where R is a bulky organic spacer cation (e.g., butylammonium (BA^+) or phenylethylammonium (PEA^+)), A is a small monovalent cation, B is a metal cation, X is a halide anion, and n represents the number of inorganic octahedral layers sandwiched between adjacent organic spacer layers.[10] However, their layered quantum-well structure also gives rise to complex crystallization behavior, multiphase coexistence, and anisotropic charge transport. In practical 2D RPP films, phases with different n values usually coexist even when the precursor composition is designed with a nominal $\langle n \rangle$ value.[11,12] The resulting phase distribution and crystal orientation strongly influence vertical charge transport and carrier extraction and, consequently, device performance.[13,14]

Various strategies have been explored in the past few years to pursue the ordered alignment of 2D RPP slabs within 2D RPP films, leading to a significant PCE enhancement of 2D-PSCs from below 10% to approaching 22%, albeit they still lag behind that of 3D-PSCs ($\sim$ 27%).[15–19] Most studies have focused on vertical phase distribution and crystal orientation profiles, whereas lateral heterogeneity, particularly at buried interfaces, has received comparatively less attention.[20,21] In our previous work, we proposed

†Corresponding author. E-mail: huziyang@nbu.edu.cn
‡Corresponding author. E-mail: zhengfei@nbu.edu.cn

© 2026 Chinese Physical Society and IOP Publishing Ltd. All rights, including for text and data mining, AI training, and similar technologies, are reserved.

that mesoscopic scale Brownian tree-shaped phase domains generally appear in high-quality 2D RPP films, which are formed by the diffusion-limited-aggregation (DLA) of large-n phase-dominated grains during film crystallization.[22] They were also identified as optical manifestations of the buried-interface void networks, and the associated morphological heterogeneity coincided with spatially heterogeneous optoelectronic responses.[23,24] However, strategies to effectively manipulate this Brownian tree-shaped crystalline lateral heterogeneity have not been systematically examined. In particular, the coupling between crystalline quality, crystal orientation, and effective buried-interface contact remains unclear. Moreover, how this crystalline morphology governs local electrical heterogeneity and macroscopic photovoltaic performance requires further investigation. A systematic investigation of this crystallization–morphology–device relationship is therefore needed to overcome the PCE bottleneck of 2D-PSCs.

Herein, we employ solvent engineering to delay the crystallization of 2D RPP films and systematically investigate the evolution of Brownian tree-shaped lateral heterogeneity and its opto-electronic responses. Increasing the DMSO fraction slows down the crystallization process of 2D RPP films, leading to improved crystalline quality and preferred vertical crystal orientation. However, this delayed crystallization is also accompanied by the development of Brownian tree-shaped crystalline domains and associated void networks at the buried interface. These void networks reduce effective buried-interface contact, thereby compromising carrier transport and collection. By correlating the Brownian tree-shaped morphology with microscale current–voltage response under illumination, a direct link between local electrical heterogeneity and photovoltaic performance was established. A DMF:DMSO ratio of 8:2 achieves a balance between crystalline quality and buried-interface contact, yielding 2D RPP films with moderate lateral heterogeneity and 2D-PSCs with an improved PCE of 17.63%.

2. Results and discussion

2D $BA_2MA_{n-1}Pb_nI_{3n+1}$ ($\langle n\rangle = 5$) RPP films prepared by hot casting from precursor solutions containing DMF:DMSO solvent mixtures were selected as prototypes to investigate the effectiveness of solvent engineering in manipulating the lateral heterogeneity of 2D RPP films. Figures 1(a)–1(d) present reflection optical microscopy images of 2D RPP films prepared with different DMF:DMSO ratios, which were acquired from the buried side through the glass substrate. As shown in Fig. 1(a), the film prepared with DMF:DMSO = 10:0 exhibits small Brownian tree-shaped domains with relatively weak optical contrast. With increasing DMSO content, the Brownian tree-shaped domains progressively enlarge laterally at solvent ratios of 9:1, 8:2, and 7:3, accompanied by increasingly distinct reflection contrast. The variation in reflected color may be related to local differences in phase distribution and the extent of void formation at the buried interface. Large-area buried-side optical microscopy images (Fig. S1) further confirm a consistent growth and expansion trend of the Brownian tree-shaped morphology. Together, these observations demonstrate the strong dependence of the lateral heterogeneity associated with crystalline morphology of 2D RPP films on the solvent composition of the precursors. According to the literature, increasing the DMSO content in the DMF:DMSO solvent mixture would slow down the crystallization speed of 3D perovskite films.[25–27] In our case, the slower crystallization speed induced by higher DMSO fraction well explains the larger Brownian tree-shaped domains observed in 2D RPP films, as these domains have more time to grow through the DLA process before film solidification.

X-ray diffraction (XRD) measurements were subsequently conducted to examine the crystalline properties of 2D RPP films accompanying the evolution of Brownian tree-shaped lateral heterogeneity. As shown in Fig. 1(e), all films exhibit two dominant diffraction peaks at approximately 14.2° and 28.4°, which can be assigned to diffraction of the (111) and (202) lattice planes of 2D RPPs, respectively. No obvious additional diffraction peaks were detected. This implies that 2D RPP microcrystal slabs in all films are mainly vertically oriented relative to the substrates, which is critical for the vertical charge transport in photovoltaic applications.[7,28,29] The corresponding peak-intensity evolution is summarized in Fig. S2. With increasing DMSO content, the intensities of both the (111) and (202) diffraction peaks gradually increase. Meanwhile, both diffraction peaks become progressively sharper, accompanied by a continuous decrease in their full width at half maximum (FWHM) values (Fig. 1(f)). These results indicate enhanced crystallinity and a more pronounced preferred vertical crystal orientation for 2D RPP films. It can thus be inferred that a higher DMSO fraction sufficiently improves the crystalline quality of 2D RPPs, thereby facilitating carrier transport through the perovskite bulk.[30]

To clarify the structure of the Brownian tree-shaped optical domains, the buried interface of the 7:3 film was exposed by mechanical delamination and examined by SEM. Details of the mechanical delamination procedure are illustrated in Fig. S3. The low-magnification SEM image in Fig. 1(g) shows that the Brownian tree-shaped interfacial areas possess brighter contrast than the rest of the view, implying stronger electron scattering from these sites. At higher magnification, the Brownian tree-shaped region (on-tree) exhibits densely interwoven void networks and locally discontinuous buried-interface contact (Fig. 1(h)). In contrast, the adjacent regions (off-tree) display a comparatively continuous buried interface with substantially fewer void features (Fig. 1(i)). These results demonstrate that the Brownian tree-shaped optical do-

mains represent regions with a greater extent of interconnected void networks at the buried interface. This observation is consistent with our previous findings on the structural origin of Brownian tree-shaped crystalline morphology at the buried interface.[22–24]

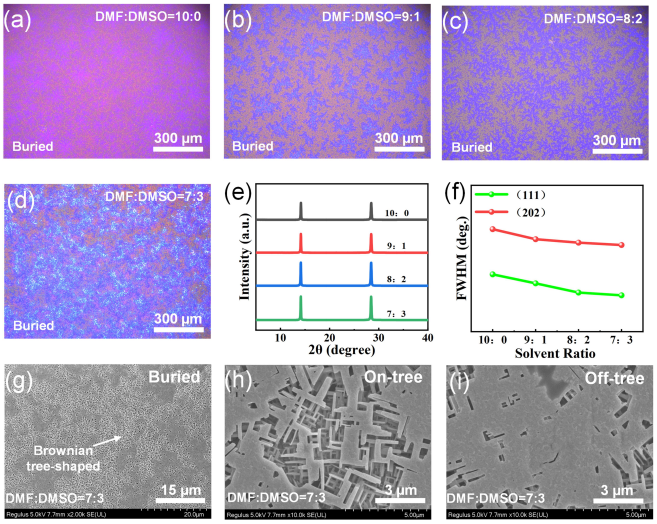

Fig. 1. Coupled evolution of Brownian tree-shaped crystalline morphology, crystallinity, and buried-interface structure in 2D RPP films. (a)–(d) Buried-side reflection mode optical microscopy images of films prepared with DMF:DMSO ratios of (a) 10:0, (b) 9:1, (c) 8:2, and (d) 7:3. (e) XRD patterns of the corresponding films. (f) FWHM values of the (111) and (202) diffraction peaks as a function of DMF:DMSO ratio. (g) Low-magnification SEM image of the mechanically exposed buried interface of the 7:3 film. High-magnification SEM images of (h) a Brownian-tree region and (i) an adjacent non-tree region. The mechanical delamination procedure is illustrated in Fig. S3.

Having established that delayed crystallization induced crystalline quality enhancement is accompanied by the development of the Brownian tree-shaped domains at the buried interface, we next examined the top-surface morphology of 2D RPP films prepared with different solvent conditions. As shown in Fig. 2(a), the film with DMF:DMSO = 10:0 exhibits a rough and granular surface with poorly developed lateral grain interconnection, indicating limited grain growth under rapid crystallization. Upon DMSO incorporation, the granular features are substantially reduced and the surface becomes more continuous. The 9:1 film shows improved grain development with more distinguishable grain boundaries (Fig. 2(b)). When the DMF:DMSO ratio is adjusted to 8:2, the film exhibits well-developed grains with relatively uniform grain interiors and clearly defined grain boundaries, giving rise to the most compact and homogeneous top-surface morphology among the investigated conditions (Fig. 2(c)). Further increasing the DMSO fraction to 7:3 preserves the large-grain morphology. However, localized contrast variations along selected grain boundaries become more apparent (Fig. 2(d)), indicating that excessive crystallization delay does not further improve film uniformity. Thus, although DMSO incorporation promotes grain development and preferred crystal orientation, excessive DMSO induces additional morphological heterogeneity.

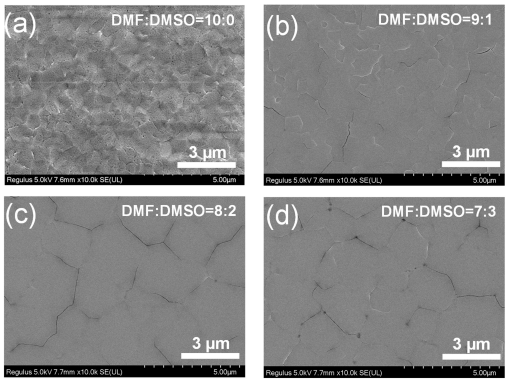

Fig. 2. Top-surface morphology evolution of 2D RPP films prepared with different DMF:DMSO ratios. Top-view SEM images of films prepared with DMF:DMSO ratios of (a) 10:0, (b) 9:1, (c) 8:2, and (d) 7:3.

To further investigate the evolution of grain topography and its correlation with the local surface potential, AFM and Kelvin probe force microscopy (KPFM) measurements were performed on corresponding regions of 2D RPP films deposited on ITO substrates. As shown in Figs. 3(a)–3(d), the film prepared with DMF:DMSO = 10:0 exhibits pronounced intragrain height fluctuations, resulting in a relatively high root-mean-square roughness (Rq) of 12.4 nm. Upon DMSO incorporation, the grains become more fully developed and the intragrain topography becomes progressively smoother. The Rq value decreases slightly to 12.1 nm for the 9:1 film and reaches the lowest value of 9.01 nm for the 8:2 film, indicating improved grain development and surface planarization. When the DMSO fraction is further increased to 7:3, the large-grain morphology is retained; however, the Rq value increases to 11.3 nm, indicating that further DMSO incorporation does not improve topographic uniformity.

The corresponding KPFM maps in Figs. 3(e)–3(h) further reveal the evolution of the surface potential distribution. The 10:0 film exhibits pronounced contact potential difference (CPD) variations within individual grains, spatially coinciding with the intragrain height fluctuations observed in the corresponding AFM image. Upon DMSO incorporation, the CPD contrast associated with intragrain morphological variation gradually weakens. In particular, the 8:2 film exhibits a more homogeneous CPD distribution across representative grain regions, consistent with its smoother intragrain topography. The 7:3 film retains a relatively continuous CPD distribution; however, its increased roughness indicates no further improvement in topographic uniformity. To further clarify the relationship between grain morphology and local CPD variation, height and CPD line profiles were extracted along the marked lines in the corresponding AFM and KPFM images. The shaded regions in Figs. 3(i)–3(l) denote representative individual grains. For the 10:0 film, the selected grain shows substantial height variation accompanied

by pronounced CPD fluctuation, supporting the correlation between intragrain morphology and local surface-potential variation.[31] In contrast, the 8:2 film exhibits the smallest height fluctuation and the smoothest CPD profile within the selected grain region. These results show that moderate solvent regulation promotes grain development and surface planarization while weakening morphology-dependent local potential perturbations.

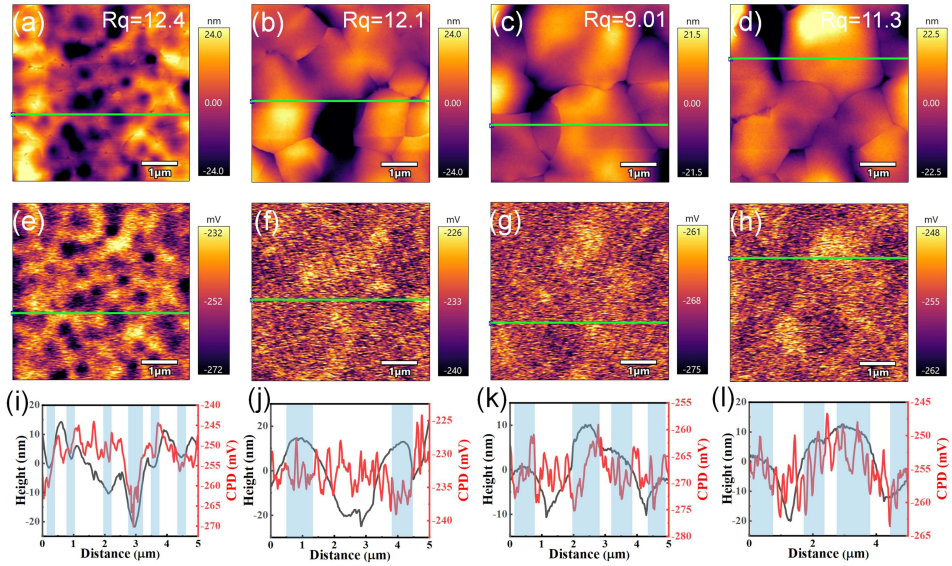

Fig. 3. Surface topography and local CPD distribution of 2D RPP films. (a)–(d) AFM height images and (e)–(h) corresponding KPFM maps of films prepared with DMF:DMSO ratios of (a), (e) 10:0, (b), (f) 9:1, (c), (g) 8:2, and (d), (h) 7:3. (i)–(l) Height and CPD line profiles extracted along the marked lines in the corresponding AFM and KPFM images.

The solvent-dependent photo-physical properties of 2D RPP films were characterized by UV–vis absorption and photoluminescence (PL) measurements. As shown in Fig. 4(a), the film prepared with DMF:DMSO = 10:0 exhibits characteristic excitonic absorption features associated with small-n phases, including $n = 2$, 3, 4, together with the absorption onset of the large-n ($n = L$) phase around 750 nm, confirming the multi-phase nature of the 2D RPP films. Upon DMSO incorporation, the absorption peak associated with the $n = 2$ phase progressively weakens and becomes indistinguishable at higher DMSO fractions. Meanwhile, the overall absorption profile changes markedly, suggesting that DMSO regulates the phase distribution during the crystallization of 2D RPP films. This phase-related optical evolution may also contribute to the reflected-color variation observed in the buried-side optical images in Fig. 1.

The corresponding top-surface PL spectra show pronounced solvent-dependent variations in both emission intensity and peak position (Figs. 4(b) and 4(c)). The PL intensity increases from the 10:0 film to the 8:2 film, with the 8:2 film exhibiting the strongest emission. In contrast, further increasing the DMSO fraction to 7:3 results in pronounced PL quenching. Meanwhile, the normalized PL spectra exhibit a progressive redshift of the emission maximum from 755 nm for the 10:0 film to 758 nm, 763 nm, and 765 nm for the 9:1, 8:2, and 7:3 films, respectively. This redshift indicates that delayed crystallization can induce an increase in the average slab thickness of the surface large-n emissive phase.[32] This is consistent with the development of the Brownian tree-shaped domains, which are composed of large-n phase-dominated grains.

As the steady-state PL intensity is governed by the competition between radiative and nonradiative recombination, time-resolved photoluminescence (TRPL) measurements were subsequently performed to probe carrier recombination dynamics. As shown in Fig. 4(d), the extracted PL lifetime increases from 122 ns for the 10:0 film to 135 ns for the 9:1 film and further to 184 ns for the 8:2 film. Together with the enhanced PL intensity, the prolonged lifetime of the 8:2 film indicates suppressed nonradiative recombination. In contrast, the 7:3 film exhibits a sharply shortened lifetime of 31 ns, indicating accelerated nonradiative decay under excessive DMSO incorporation. The spatially resolved luminescence distribution was further examined by PL mapping. As shown in Figs. 4(e)–4(h), the 10:0 film exhibits predominantly moderate photon-count regions, whereas the 9:1 and 8:2 films display increasingly extensive high-photon-count regions. The 8:2 film shows the strongest photon-count response over a large area, consistent with its enhanced steady-state PL emission and prolonged PL lifetime. In contrast, the 7:3 film is dominated by weak-emission regions with only sparse high-intensity spots. Notably, the severe PL quenching in the 7:3 film can be attributed to pronounced nonradiative recombination caused by the buried interfacial defects at the regions with enlarged void networks (Figs. 1(d), 1(h), and 1(i)).[33–35]

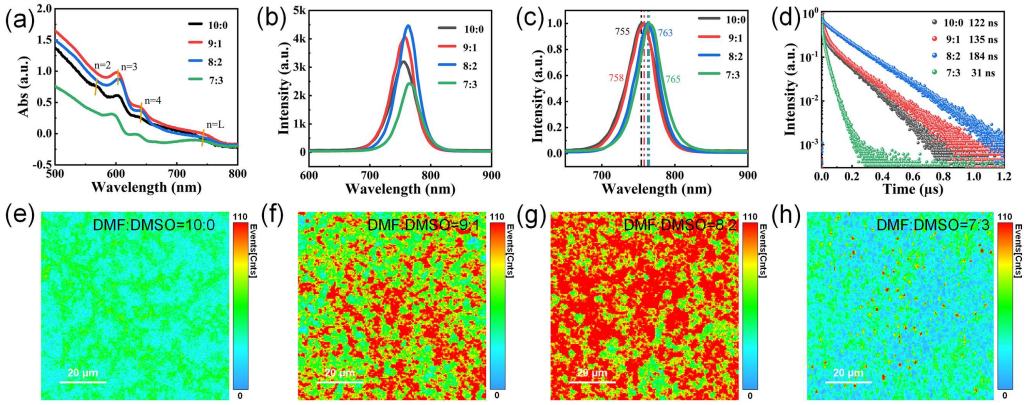

Fig. 4. Solvent-dependent photo-physical properties of 2D RPP films. (a) UV–vis absorption spectra. (b) Top-surface PL spectra. (c) Normalized top-surface PL spectra. (d) TRPL decay profiles and extracted PL lifetimes. (e)–(h) Top-surface PL photon-count maps of films prepared with DMF:DMSO ratios of (e) 10:0, (f) 9:1, (g) 8:2, and (h) 7:3.

To further investigate the electrical response of Brownian tree-shaped domains upon solvent engineering, p–i–n type 2D-PSCs with an architecture of ITO/SAM/$BA_2MA_{n-1}Pb_nI_{3n+1}$ ($\langle n\rangle = 5$)/PCBM/BCP/Ag were fabricated (Fig. 5(a)). The setup of local current–voltage (I–V) measurement of the completed photovoltaic devices is provided in Fig. 5(b). Local I–V measurements were conducted under 450 nm laser illumination at identical excitation power to compare the electrical responses of Brownian tree-shaped (on-tree) regions and adjacent off-tree regions within the same device. As shown in Figs. 5(c)–5(f), points A–D denote measurement positions within Brownian tree-shaped domains for devices prepared with DMF:DMSO ratios of 10:0, 9:1, 8:2, and 7:3, respectively, whereas points A′–D′ represent the corresponding adjacent off-tree film regions. Representative localized I–V curves acquired at these positions upon laser illumination are shown in Figs. 5(g)–5(j). From 10:0 to 8:2, the short-circuit current (I_{SC}, at 0 V) increases in both regions, rising from 154 nA to 330 nA and 425 nA in the off-tree regions and from 97 nA to 207 nA and 263 nA in the corresponding on-tree regions. In contrast, for the 7:3 device, the current in the Brownian tree-shaped region decreases sharply to 55 nA, whereas that in the adjacent off-tree region remains at 301 nA. Notably, the short-circuit current values acquired at the on-tree regions are substantially lower than those at the off-tree regions for all 2D RPP films prepared under different solvent conditions, demonstrating that the buried-interface void networks associated with the Brownian tree-shaped crystalline domains severely hinder local charge transport and collection.

To quantify the local current loss revealed by the representative localized I–V curves, the current difference between the adjacent off-tree and Brownian tree-shaped regions was defined as ΔI. The normalized local current loss, η_{loss}, was calculated as

$$\eta_{loss} = \frac{I_{off-tree} - I_{on-tree}}{I_{off-tree}} \times 100\%,$$

wherein $I_{off-tree}$ and $I_{on-tree}$ denote the local I_{SC} in the adjacent off-tree and Brownian tree-shaped (on-tree) regions, respectively. The resulting solvent-dependent ΔI and η_{loss} values are summarized in Fig. S4. Specifically, ΔI increases from 57 nA for the 10:0 device to 123 nA, 162 nA, and 246 nA for the 9:1, 8:2, and 7:3 devices, respectively (Fig. S4(a)), whereas η_{loss} remains nearly constant at approximately 37%–38% from 10:0 to 8:2 before increasing sharply to 81.7% at 7:3 (Fig. S4(b)). From 10:0 to 8:2, both on-tree and off-tree currents increase while η_{loss} remains nearly unchanged, indicating that the enhancement in carrier transport arising from improved crystallinity and preferred vertical orientation outweighs the adverse effect of the progressively developing buried-interface void networks on charge collection. In contrast, the sharp increase in η_{loss} at 7:3 indicates that the extensive development of the Brownian tree-shaped morphology and associated buried-interface void defects becomes the dominant factor limiting local charge collection. To verify the reproducibility of the local electrical contrast, statistical localized I–V measurements were further performed using 20 Brownian tree-shaped regions and 20 adjacent off-tree regions for each solvent condition. In addition to the lower current response, the Brownian tree-shaped regions also exhibit lower local open-circuit voltage (V_{OC}) values than the adjacent off-tree regions, suggesting stronger nonradiative recombination-induced voltage losses associated with the enlarged buried-interface void defects.[36] The corresponding current and voltage distributions are summarized in Fig. S5, revealing consistently weaker electrical responses in Brownian tree-shaped regions. These statistical results corroborate the representative localized I–V measurements and confirm that the local electrical loss associated with the Brownian tree-shaped morphology is reproducible.

To further assess how the spatial contribution of Brownian tree-shaped regions affects the device-level response, their areal coverage was semi-quantitatively estimated from the optical images in Figs. 5(c)–5(f) (Fig. S6). The estimated areal fraction progressively increases with increasing DMSO content (Fig. S7), consistent with the growth and expansion trend observed in the large-area buried-side optical images (Fig. S1).

Considering the substantially lower charge-collection capability of the Brownian tree-shaped regions, their increasing areal coverage is expected to aggravate the overall photocurrent loss. The macroscopic photovoltaic performance was therefore evaluated for 2D-PSCs with the same device architecture prepared under different DMF:DMSO ratios. Representative current density–voltage (J–V) curves are shown in Fig. 5(k), and the corresponding photovoltaic parameters are summarized in Table 1. The J_{SC} increases from 10:0 to 8:2 and then decreases markedly at 7:3. This evolution is consistent with the collective contribution of spatially distributed regions with different charge-collection efficiencies. Thus, the increasing spatial contribution of Brownian tree-shaped regions with inferior local charge collection can contribute to the macroscopic J_{SC} loss.[37,38]

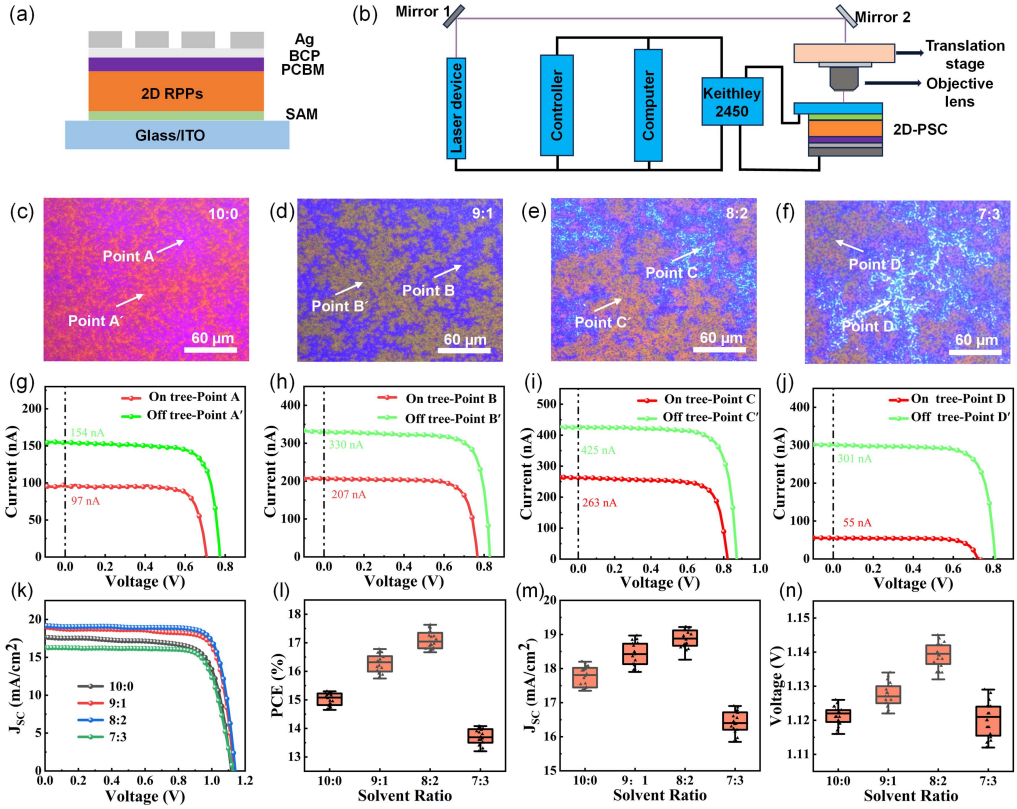

Fig. 5. Correlation between Brownian tree-shaped morphology, local electrical response, and macroscopic photovoltaic performance in 2D-PSCs. (a) Schematic illustration of the device architecture. (b) Schematic of the localized illuminated current–voltage measurement setup. (c)–(f) Buried-side reflection optical images of 2D-PSCs based on 2D RPP films with DMF:DMSO ratios of (c) 10:0, (d) 9:1, (e) 8:2, and (f) 7:3. (g)–(j) Representative localized illuminated I–V curves. (k) Representative J–V curves of the champion 2D-PSCs. Statistical distributions of (l) PCE, (m) J_{SC}, and (n) V_{OC} of 2D-PSCs.

Table 1. Performance parameters of champion 2D-PSC devices based on 2D RPP films prepared with different DMF:DMSO ratios.

Sample	V_{OC} (V)	J_{SC} (mA/cm^2)	FF (%)	PCE (%)
10:0	1.124	18.20	74.69	15.27
9:1	1.134	18.97	78.00	16.78
8:2	1.144	19.22	80.22	17.63
7:3	1.126	16.31	76.75	14.10

The statistical distributions of power conversion efficiency (PCE), short-circuit current density (J_{SC}), and open-circuit voltage (V_{OC}) are presented in Figs. 5(l)–5(n). With increasing DMSO content, all three parameters progressively improve and reach their optimal values at 8:2, followed by a clear decrease at 7:3. A similar trend is observed in the long-term ambient storage stability (Fig. S8). After 480 h of storage in air, the unencapsulated devices with DMF:DMSO ratios of 10:0, 9:1, 8:2, and 7:3 retain approximately 83%, 87%, 94%, and 71% of their initial PCEs, respectively. The 8:2 devices show the highest PCE retention, whereas the 7:3 devices undergo the most severe degradation. This difference may be related to the extensive buried-interface void networks at 7:3, which weaken interface integrity and increase the susceptibility of the device to environmental degradation. Combined with the localized electrical results, these trends indicate that moderately delayed crystallization improves charge transport and collection through enhanced crystalline quality and preferred crystal orientation, while the extensive development of the Brownian tree-shaped crystalline domains at 7:3 is accompanied by enlarged buried-interface void defects and aggravated local electrical losses. Therefore, optimal device performance is achieved by balancing crystalline quality and preferred crystal orientation with effective buried-interface contact.

Finally, Fig. 6 schematically summarizes the solvent-regulated crystallization mechanism and the resulting trade-

off between bulk structural improvement and buried-interface integrity in 2D RPP films. At DMF:DMSO = 10:0, rapid crystallization limits grain development and lateral coalescence, resulting in lower crystalline quality and weaker preferred crystal orientation. The 9:1 condition shows an intermediate crystallization state between the 10:0 and 8:2 conditions and is therefore not treated as a distinct crystallization regime. At 8:2, moderately delayed crystallization improves the crystalline quality and preferred vertical orientation, facilitating carrier transport through the perovskite bulk. Meanwhile, the Brownian tree-shaped domains and associated buried-interface void networks also become more developed, but their extent remains moderate, allowing sufficient buried-interface contact for efficient charge collection. In contrast, further increasing the DMSO fraction to 7:3 promotes extensive expansion of the Brownian tree-shaped domains and buried-interface void networks. The resulting deterioration of buried-interface contact causes pronounced local charge-collection losses, which outweigh the benefits of the improved bulk structural properties and lead to reduced device performance. These results demonstrate that optimal performance requires a balance between improved crystallinity and preferred crystal orientation and preserved buried-interface contact, rather than maximizing crystallinity alone.

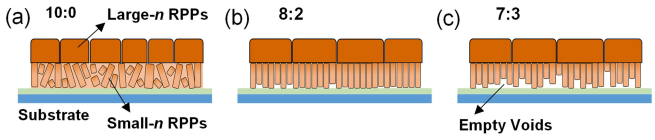

Fig. 6. Solvent-regulated crystallization in 2D RPP films. (a) Rapid crystallization at DMF:DMSO = 10:0. (b) Moderately delayed crystallization at DMF:DMSO = 8:2. (c) Excessive delayed crystallization at DMF:DMSO = 7:3.

3. Conclusion

In summary, this work reveals that delayed crystallization in 2D RPP films improves crystalline quality and preferred crystal orientation while simultaneously promoting the development of Brownian tree-shaped lateral heterogeneity. The expansion of Brownian tree-shaped domains is associated with enlarged buried-interface void networks and pronounced local electrical heterogeneity. Based on localized illuminated current–voltage measurements, this work establishes a direct correlation between crystalline morphology at the buried interface, local electrical response, and photovoltaic performance. A DMF:DMSO ratio of 8:2 achieves a balance between improved crystallinity and effective buried-interface contact, yielding 2D-PSCs with an improved PCE of 17.63%. These findings highlight the importance of controlling lateral heterogeneity and suppressing Brownian tree-shaped void networks to preserve buried-interface integrity, thereby improving the performance potential of 2D-PSCs.

Acknowledgements

This work was supported by the National Natural Science Foundation of China (Grant Nos. 62304116, 62074088, and 62174094), and the Public Welfare Science and Technology Plan Project of Ningbo (Grant No. 2025S109). The author Z. Hu would like to thank the sponsorship by K.C. Wong Magna Fund in Ningbo University. K.P.G. acknowledges the funding support from the ARC Centre of Excellence in Exciton Science (Grant No. CE170100026).

References

[1] Jena A K, Kulkarni A and Miyasaka T 2019 *Chem. Rev.* **119** 3036
[2] Park N G and Zhu K 2020 *Nat. Rev. Mater.* **5** 333
[3] Shi P, Ding Y, Ding B, *et al*. 2023 *Nature* **620** 323
[4] Khenkin M V, Katz E A, Abate A, *et al*. 2020 *Nat. Energy* **5** 35
[5] Berhe T A, Su W N, Chen C H, Pan C J, Cheng J H, Chen H M, Tsai M C, Chen L Y, Dubale A A and Hwang B J 2016 *Energy Environ. Sci.* **9** 323
[6] Li X, Hoffman J M and Kanatzidis M G 2021 *Chem. Rev.* **121** 2230
[7] Tsai H, Nie W, Blancon J C, Stoumpos C C, Asadpour R, Harutyunyan B, Neukirch A J, Verduzco R, Crochet J J, Tretiak S, Pedesseau L, Even J, Alam M A, Gupta G, Lou J, Ajayan P M, Bedzyk M J, Kanatzidis M G and Mohite A D 2016 *Nature* **536** 312
[8] Sirbu D, Balogun F H, Milot R L and Docampo P 2021 *Adv. Energy Mater.* **11** 2003877
[9] Calado P, Telford A M, Bryant D, Li X, Nelson J, O'Regan B C and Barnes P R F 2016 *Nat. Commun.* **7** 13831
[10] Zhang F, Lu H, Tong J, Berry J J, Beard M C and Zhu K 2020 *Energy Environ. Sci.* **13** 1154
[11] Qiu J, Zheng Y, Xia Y, Chao L, Chen Y and Huang W 2019 *Adv. Funct. Mater.* **29** 1806831
[12] Zhang X, Munir R, Xu Z, Liu Y, Tsai H, Nie W, Li J, Niu T, Smilgies D M, Kanatzidis M G, Mohite A D, Zhao K, Amassian A and Liu S F 2018 *Adv. Mater.* **30** 1707166
[13] Proppe A H, Quintero-Bermudez R, Tan H, Voznyy O, Kelley S O and Sargent E H 2018 *J. Am. Chem. Soc.* **140** 2890
[14] Chen A Z, Shiu M, Ma J H, Alpert M R, Zhang D, Foley B J, Smilgies D M, Lee S-H and Choi J J 2018 *Nat. Commun.* **9** 1336
[15] Qian W, Dai S, Wang H, Hu T, Liu K, Wang Y, Guo Q, Yue X, Wang Y, Li C, Hu Z, Liu R, Qin S, Wang J, Qin J, Zhang J, Yu A and Zhan Y 2025 *ACS Appl. Mater. Interfaces* **17** 16932
[16] Xiong Z, Zhang Q, Cai K, Zhou H, Song Q, Han Z, Kang S, Li Y, Jiang Q, Zhang X and You J 2025 *Science* **390** 638
[17] Li B, Ding J, Zhang Z, Li M, Li C, Wu W, Lu M, Liu H, Lin Z, Pauport T and Chen C 2026 *Adv. Mater.* **38** e73807
[18] Feng W, Wang R, Ye Y, Guo Z, Wang P, Li Y, Chen Y, Hu Z and Liu Y 2026 *Angew. Chem. Int. Ed.* **65** e4293157
[19] Huang N, Wang D, Fang J, Wang X, Gong S, Li S, Xie G, Li H, Lin D, Gan L, Peng H, Chen X, He S and Qiu L 2025 *ACS Nano* **19** 13427
[20] Gao G, Dong Y, Jiang L, Liu Q, Liu X, Chen Q, Wang T and Zhu T 2024 *Nano Lett.* **24** 13356
[21] Zeng F, Su Z, Kong W, Li F, Liang Y, Zhang X, Wang T, Zhang L, Lvtao Y, Liu R, Gao X, Huang J, Yang X and Zheng R 2024 *Energy Environ. Sci.* **17** 8284
[22] Zheng F, Angmo D, Hall C R, Rubanov S, Yuan F, Laird J S, Gao M, Smith T A and Ghiggino K P 2022 *Adv. Mater. Interfaces* **9** 2102231
[23] Zheng F, Rubanov S, Hall C, Liu J, Gao M, Smith T A, Angmo D and Ghiggino K P 2025 *Adv. Mater. Interfaces* **12** 2401012
[24] Zheng F, Raeber T, Rubanov S, Lee C, Seeber A, Hall C, Smith T A, Gao M, Angmo D and Ghiggino K P 2022 *ACS Appl. Mater. Interfaces* **14** 51910
[25] Jiang J, Vicent-Luna J M and Tao S 2022 *J. Energy Chem.* **68** 393
[26] Telschow O, Scheffczyk N, Hinderhofer A, Merten L, Kneschaurek E, Bertram F, Zhou Q, Löffler M, Schreiber F, Paulus F and Vaynzof Y 2023 *Adv. Sci.* **10** 2206325
[27] Bautista-Quijano J R, Telschow O, Paulus F and Vaynzof Y 2023 *Chem. Commun.* **59** 10588

[28] Hou Y, Zheng F, Yang L, Qi X, Ma G, Luo Z, Zhao Z, Wang X, Zhao Z and Hu Z 2025 *ACS Appl. Mater. Interfaces* **17** 3806
[29] Zheng F, Zuo C, Niu M, Zhou C, Bradley S J, Hall C R, Xu W, Wen X, Hao X, Gao M, Smith T A and Ghiggino K P 2020 *ACS Appl. Mater. Interfaces* **12** 25980
[30] Yang Y, Liu C, Mahata A, Li M, Roldán-Carmona C, Ding Y, Arain Z, Xu W, Yang Y, Schouwink P A, Züttel A, De Angelis F, Dai S and Nazeeruddin M K 2020 *Energy Environ. Sci.* **13** 3093
[31] Yang B, Zheng F, Hou Y, Wang P, Sheng L, Chen X, Shafique S, Zhao Z, Ghiggino K P and Hu Z 2026 *Nano Lett.* **26** 5443
[32] Zheng F, Hall C R, Angmo D, Zuo C, Rubanov S, Wen Z, Bradley S J, Hao X T, Gao M, Smith T A and Ghiggino K P 2021 *J. Mater. Chem. C* **9** 5362
[33] Chen P, Xiao Y, Li S, Jia X, Luo D, Zhang W, Snaith H J, Gong Q and Zhu R 2024 *Chem. Rev.* **124** 10623
[34] deQuilettes D W, Frohna K, Emin D, Kirchartz T, Bulovic V, Ginger D S and Stranks S D 2019 *Chem. Rev.* **119** 11007
[35] Dong X, Li X, Wang X, Zhao Y, Song W, Wang F, Xu S, Miao Z and Wu Z 2024 *Adv. Mater.* **36** 2313056
[36] Correa-Baena J P, Tress W, Domanski K, Anaraki E H, Turren-Cruz S-H, Roose B, Boix P P, Grätzel M, Saliba M, Abate A and Hagfeldt A 2017 *Energy Environ. Sci.* **10** 1207
[37] Zhao X, Wang Z, Tian W, Yan X, Shi Y, Wang Y, Sun Z and Jin S 2022 *J. Energy Chem.* **72** 8
[38] Leblebici S Y, Leppert L, Li Y, *et al*. 2016 *Nat. Energy* **1** 16093